Spatial Variations of Polarized Synchrotron Emission in the QUIJOTE MFI Data

J. M. Casas[1,2], L. Bonavera[3,4], J. González-Nuevo[3,4], J. A. Rubiño-Martín[1,2], R. T. Génova-Santos[1,2], R. B. Barreiro[5], M. M. Cueli[6,7], D. Crespo[3,4], R. Fernández-Fernández[3,4], J. A. Cano[3,4]

[1]Instituto de Astrofísica de Canarias, E-38205 La Laguna, Tenerife, Spain
[2]Universidad de La Laguna, Departamento de Astrofísica, E-38206 La Laguna, Tenerife, Spain
[3]Universidad de Oviedo, Departamento de Física, C. Federico García Lorca 18, 33007 Oviedo, Spain
[4]Instituto Universitario de Ciencias y Tecnologías Espaciales de Asturias (ICTEA), C. Independencia 13, 33004 Oviedo, Spain
[5]Instituto de Física de Cantabria (IFCA), CSIC-Univ. de Cantabria, Avenida los Castros, s/n, E-39005 Santander, Spain
[6]SISSA, Via Bonomea 265, 34136 Trieste, Italy
[7]IFPU - Institute for fundamental physics of the Universe, Via Beirut 2, 34014 Trieste, Italy

ABSTRACT

Polarized synchrotron emission from ultra-relativistic electrons spiraling the Galactic magnetic field has become one of the most relevant emissions in the Interstellar medium these last years due to the improvement in the quality of low-frequency observations. One of the recent experiments designed to explore this emission is the QUIJOTE experiment.

In this work, we aim to study the spatial variations of the synchrotron emission in the QUIJOTE MFI data, by dividing the sky into physically separated regions. For such task, we firstly use a novel component separation method based on artificial neural networks to clean the synchrotron maps. After training the network with simulations, we fit both EE and BB spectra by assuming a power-law model. Then, we give estimations for the index α_S, the amplitude, and the ratio between B and E amplitudes.

When analyzing the real data, we found a clear spatial variation of the synchrotron properties along the sky at 11 GHz, consistent with previous analyses, obtaining a steeper index in the Galactic plane of $\alpha_S^{EE} = -3.1 \pm 0.3$ and $\alpha_S^{BB} = -3.1 \pm 0.4$ and a flatter one at high Galactic latitudes of $\alpha_S^{EE} = -3.05 \pm 0.2$ and $\alpha_S^{B} = -2.98 \pm 0.27$. We found average values at all sky of $\alpha_S^{EE} = -3.04 \pm 0.21$ and $\alpha_S^{BB} = -3.00 \pm 0.34$. Furthermore, after obtaining an average value of $A_S^{EE} = 3.31 \pm 0.08\,\mu K^2$ and $A_S^{BB} = 0.93 \pm 0.02\,\mu K^2$, we estimate a ratio between B and E amplitudes of $A_S^{BB}/A_S^{EE} = 0.28 \pm 0.08$.

Based on the results we conclude that, although neural networks seem to be valuable methods to apply on real ISM observations and in future QUIJOTE MFI2 data, combined analyses with *Planck*, WMAP and/or CBASS data are mandatory to reduce the noise contamination from QUIJOTE estimated maps and then improve the accuracy of the estimations.

Key words. ISM: general – Galaxy: general – cosmic background radiation–cosmology: observations – diffuse radiation

. Introduction

he interstellar medium (ISM) is a complex physical system here several emissions undergo abrupt state changes when ineracting with each other and with the Galactic magnetic field Draine 2011), displaying significant variability across all scales. o characterize this complexity, phenomenological models are eveloped based on observations from ground-based and satelite experiments, as well as accurately inferring the physical beavior of these emissions at scales not yet observed (The Pan-Experiment Galactic Science Group 2025).

In recent decades, several experiments have helped constrain many properties of the ISM, especially in the microwave band. In particular, observations from the Planck satellite (Planck Collaboration et al. 2020a) have provided unprecedented, detailed maps on both the temperature and polarization emissions. While *Planck* has released detailed temperature and polarization maps of interstellar dust emission (Planck Collaboration et al. 2014, Planck Collaboration et al. 2015), which have led to improvements in theoretical models (Hensley & Draine 2021), many properties of synchrotron emission produced by ultra-relativistic electrons spiraling along the Galactic magnetic field remain poorly constrained, especially due to the lower sensitivity of the instruments measuring the lowest frequencies of the microwave spectra, although efforts have been made recently by the BeyondPlanck and COSMOGLOBE Collaborations to published refined maps of the emission (Watts et al. 2024).

In principle, polarized synchrotron emission is generally modeled by a power-law spectral behavior:

$$X_\nu = A \left(\frac{\nu}{\nu_S} \right)^{\beta_S}, \quad (1)$$

where X_ν represents each Q and U Stokes parameter maps, A_S is the brigthness temperature at the pivot frequency $\nu_S = 30$ GHz and β_S is the spectral index, which is assumed to be equal for both Q and U maps. This model emission can also be characterized by fitting both EE and/or BB spectra for a certain multipole range by following the parametrization described in Krachmalnicoff et al. (2018):

$$C_l^{XX} = A_{XX} \left(\frac{l}{80} \right)^{\alpha_{XX}}, \quad (2)$$

where $X \in \{E, B\}$, A_{XX} is the amplitude of the spectrum at the pivot multipole $l = 80$, and the index α_{XX} is the slope of the multipole dependence.

Early measurements from WMAP (e.g., Page et al. 2007; Gold et al. 2011) provided large-scale maps of synchrotron polarization and inferred a typical spectral index in polarization of $\beta_S \approx -3.0$ with significant spatial variation, especially near the Galactic plane and along filamentary structures. After that, the Planck Low Frequency Instrument (LFI) extended this analysis with improved sensitivity and resolution, giving an average index in polarization of $\beta_S \approx -3.1 \pm 0.1$, in combination with WMAP (Planck Collaboration et al. 2020b).

More recent analyses using the same observations alone or in combination with other surveys have better constrained the synchrotron parameters. Particularly, Fuskeland et al. (2014) have exploited the WMAP 23 and 33 GHz frequency channels using two parallel methodologies: T–T plots and maximum likelihood estimation across 24 sky regions physically different between them, obtaining a more constrained spatial variation in the synchrotron index, with an average of $\beta_S = -2.98 \pm 0.01$ at the Galactic plane and $\beta_S = -3.12 \pm 0.04$ at high Galactic latitudes, and with an average value at all sky of $\beta_S = -2.99 \pm 0.01$. Moreover, Krachmalnicoff et al. (2018) used the S-Band Polarization All Sky Survey (SPASS) data in the range of 2.3 and 33 GHz with several latitude cuts, finding $\alpha_S^E \approx \alpha_S^B = -2.59 \pm 0.01$, $A_S^E = 2.2 \pm 0.2 \mu K^2$, $A_S^B = 1.9 \pm 0.2 \mu K^2$ and $A_S^B/A_S^E = 0.87 \pm 0.02$ for $|b| > 20°$ (30% of the sky), and an average constant value at all sky of $\beta_S = -3.22 \pm 0.08$.

After that, Fuskeland et al. (2021) joined this data with WMAP 23 GHz one on the same regions described in Fuskeland et al. (2014), and by using a T-T plot methodology, confirming the past analyses concerning the synchrotron spatial variability along the sky, obtaining an index of $\beta_S = -2.98 \pm 0.01$ at the Galactic plane and $\beta_S = -3.12 \pm 0.04$ at high Galactic latitudes, and with an average value of $\beta_S = -3.24 \pm 0.01$ taking into account the Faraday correction.

More recent analyses, such the ones from Martire et al. (2022), Weiland et al. (2022) and Watts et al. (2024) have reached similar results. In the first case, they combined WMAP 23 GHz channel with 30 GHz *Planck* one and fitted both *EE* and *BB* spectra by assuming a power-law model as in Equations (1) and (2) for a set of six sky regions covering from 30 to 94% of the sky, and finding $\alpha_S^E = -2.95 \pm 0.04$ and $\alpha_S^B = -2.85 \pm 0.14$, with a ratio between B and E amplitudes of $r = A_S^B/A_S^E = 0.22 \pm 0.02$ for the 94% case. In the second analysis, they also found a clear spatial variability on synchrotron using SPASS, WMAP and Planck, reaching a synchrotron spectral index in the range $-3.4 \lesssim \beta_S \lesssim -3$. Finally, Watts et al. (2024) analysis, which is a reprocessed set of maps produced by the COSMOGLOBE Collaboration from all WMAP and *Planck* LFI frequency ones, led to significantly lower instrumental systematics than the legacy products from each experiment. They thus found a spectral index $\beta_S = -3.07 \pm 0.07$ at 30 GHz, and a mean ratio between B and E amplitudes of $r = A_S^B/A_S^E = 0.39 \pm 0.02$.

All these analyses have confirmed the importance of having data from several experiments with different sensitivities and coverage to be joint together, especially in the low-frequency range. This is precisely the main idea behind the QUIJOTE (Q-U-I JOint Tenerife Experiment) experiment (Rubiño-Martín et al. 2023), which have observed the northern sky between 2012 and 2018, and that it is now re-observing it with a more precise instrument called MFI2 (Hoyland et al. 2022).

QUIJOTE MFI maps have allowed to give more constrains about the synchrotron parameters, for example by fitting the *EE* and *BB* power spectra with different Galactic cuts (Rubiño-Martín et al. 2023), obtaining $\alpha_S^E = -3 \pm 0.16$ and $\alpha_S^B = -3.08 \pm 0.42$, and a ratio between B and E amplitudes of $r = A_S^B/A_S^E = 0.26 \pm 0.07$, and also by running a parametric component separation method (de la Hoz et al. 2023), reaching an average spectral index of $\beta_S = -3.08 \pm 0.13$.

In this work, we aim to extend the findings of these two approaches by investigating more about the spatial variability of the polarized synchrotron emission in the public QUIJOTE MFI observations with the use of a novel component separation method based on artificial neural networks, initially presented in Casas et al. (2022), for separating the cosmic microwave background (CMB) in temperature maps, and thus extended to polarization CMB maps in Casas et al. (2023). The main motivation to use this kind of methodology is the ability of neural networks to find non-trivial patterns in non-linear data, which is precisely the ones governing the physics of the microwave polarization sky. Section 2 describes the data and realistic simulations we use in this work. Section 3 summarizes the methodology. Section 4 presents the results when applying the network to both realistic simulations and observations and Section 5 shows our conclusions. Appendix A presents a summary of the theoretical framework of our component separation method, and Appendix B shows more results for completeness.

2. Data

2.1. QUIJOTE MFI observations

The QUIJOTE (Q-U-I JOint Tenerife Experiment, Rubiño-Martín et al. (2023)) project is a ground-based polarimetric experiment focused on studying the polarization of the cosmic microwave background (CMB) as well as various Galactic and extragalactic processes[1]. It operates in the 10-40 GHz frequency range and mainly targets large angular scales. The experiment is situated at the Teide Observatory in Tenerife, at an altitude of roughly 2400 meters, where meteorological conditions are highly stable for observing the sky.

QUIJOTE comprises two telescopes outfitted with three instruments: the Multi-Frequency Instrument (MFI), the Thirty-GHz Instrument (TGI), and the Forty-GHz Instrument (FGI), which observe in the 10-20 GHz, 26-36 GHz, and 39-49 GHz bands, respectively.

The MFI operated from November 2012 until October 2018, during which it carried out two types of surveys: (i) a wide-area Galactic survey covering the sky visible from Tenerife at elevations above 30°, and (ii) a deep cosmological survey spanning about 3000 square degrees across three separate regions in the northern hemisphere. These low-frequency observations are essential for improving our understanding of foreground emissions, since the instruments aboard experiments such WMAP and *Planck* could not characterized efficiently most of the relevant processes in the sky due to their sensitivities at the lowest channels.

In this work, we use the MFI observations at 11, 13, 17 and 19 GHz, which are publicly available. The 11 GHz Q sky is shown in Figure 1, left panel.

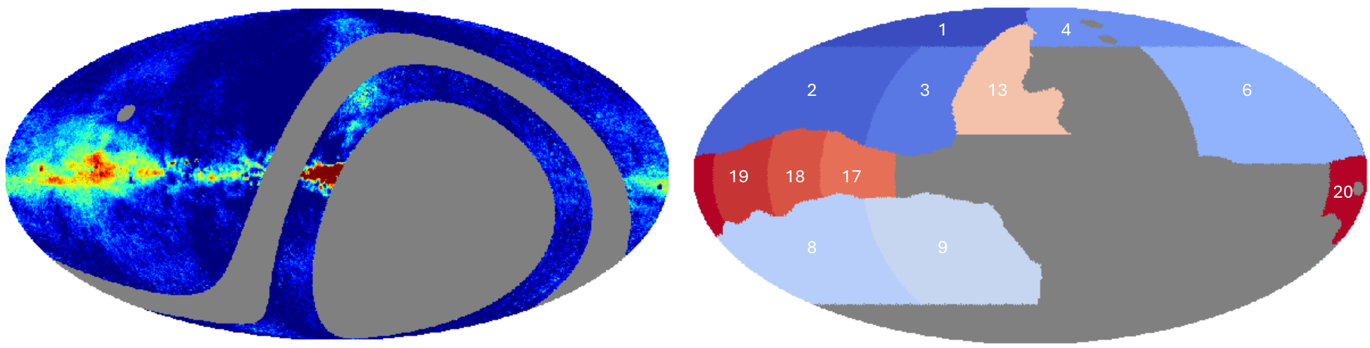

Fig. 1: Mollview projection of the data used in this work. Left panel: QUIJOTE Q MFI sky at 11 GHz. Right panel: polarized synchrotron regions defined by Fuskeland et al. (2014). It is shown in grey the regions that cannot be used in this work due to QUIJOTE coverage and patch sizes.

Table 1: Central positions in longitude and latitude ([lon, lat]) in degrees of the square patches into we divide the sky in this work. Each patch covers a total of 29.44 square degrees of the sky. The regions are the ones defined in Fuskeland et al. 2014 and displayed in Figure 1.

Region (R)	Patch position
1	[60°, 75°]
2	[160°, 45°]
3	[60°, 45°]
4	[340°, 90°]
6	[200°, 45°]
8	[120°, -30°]
9	[275°, -75°]
13	[45°, 45°]
17	[90°, 0°]
18	[135°, 0°]
19	[165°, 0°]
20	[225°, 0°]
High Galactic Latitudes (HGL)	R1 to R13
Galactic Plane (GP)	R17 to R20

2.2. QUIJOTE MFI simulations

The simulations used in this work include both Galactic and extragalactic emissions at the frequencies covered by QUIJOTE, as well as the CMB and instrumental noise consistent with QUIJOTE sensitivity levels. The CMB simulation was obtained from the Planck Legacy Archive website (PLA[2]), as a lensed realization developed from the published cosmological parameters. On the other hand, Galactic dust emission was modeled using the d10 model from the Python Sky Model (PySM, (Thorne et al. 2017)), while Galactic synchrotron emission follows the s5 model, also from PySM. This synchrotron model has the particularity that it has no curvature although having spatial variability of the spectral index along the sky inside WMAP and *Planck* observational bounds[3]. We thus have selected this model to not give the neural network prior information about curvature data, in order to evaluate if it is capable of find some insights when validating with the observations.

Anomalous microwave emission and radio point sources were added for completeness using, for the first, the a2 model from the PySM, and for the second the software CORRSKY (González-Nuevo et al. 2005) and the model by Tucci et al. (2011) in intensity, with a final extrapolation to polarization by using the estimated parameters by Bonavera et al. (2017) at low microwave frequencies.

We then generate three types of datasets: one for training the neural network, consisting on 10000 simulations, one for testing, formed by 1000 ones, and another for validation, constructed with 100 more simulations for each region. Each simulation centered on a given position (which is the same for all the 11, 13, 17, and 19 GHz QUIJOTE channels), is called Input Total patches in this work, plus the synchrotron map at 11 GHz, which is stored for each simulation as a label.

The simulations are thus constructed as follows: Firstly, a random central position at a certain position in the sky is selected for each patch. Then, the maps are cut into square patches of 256×256 pixels, with each pixel having the QUIJOTE angular resolution (approximately 6.9 arcmin). Next, point sources are injected into the patches, and a FWHM of 1° is applied. Finally, instrumental noise is added on each patch based on QUIJOTE MFI wide survey sensitivity (43.1, 38.2, 36.4 and 34.8 μK per pixel on each channel (Génova-Santos et al. 2015)), which allows us to have different realizations for each simulation.

For validation, both observations and simulations are cut into sky patches of regions physically similar but different with respect to the other ones, as described in Fuskeland et al. (2014). This allows to properly study the spectral variations on synchrotron emission across the sky. In the case of simulations, we cut 100 patches for each region. In the case of the observations, we cut a single patch for each one.

An example of the patches used in this work at 11 GHz is shown in Figure 2, being the simulated sky at the top row, left column, the observations at the same sky location at the top row, center column, and the synchrotron model at the bottom row, left column.

[1] https://research.iac.es/proyecto/quijote/
[2] http://pla.esac.esa.int/pla/#home
[3] The reader is encouraged to follow the PySM documentation in order to find more information about this: https://pysm3.readthedocs.io/en/latest/models.html

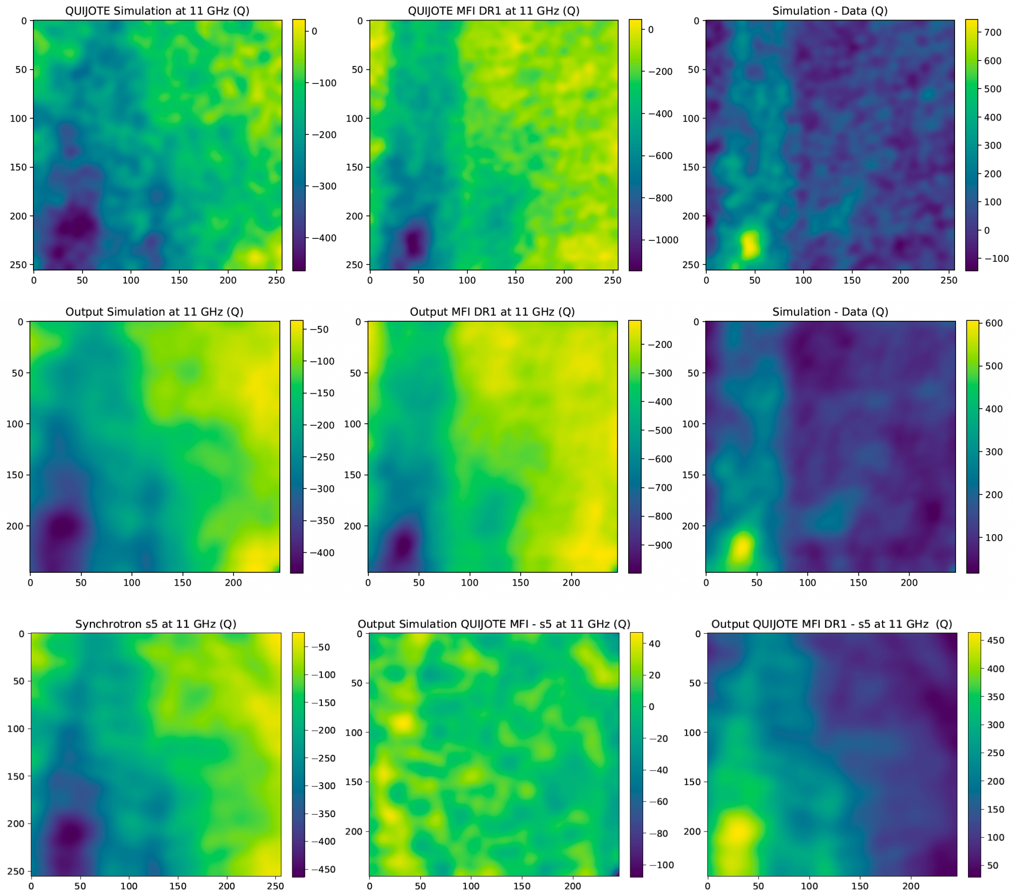

Fig. 2: Example of the kind of data we are using in this work, which represents in this case a patch of the Q sky as seen by QUIJOTE MFI in the North Polar Spur (sky Region 13) at the position [lon, lat] = [45°, 45°] for, from top to bottom and left to right: our simulations, the QUIJOTE MFI observations at 11 GHz, the difference between them, the synchrotron patch output from the neural network, the output from the same trained network but using the real data, the difference between these two last maps, the synchrotron s5 model at this sky patch and then the difference between the outputs from the network and the synchrotron model when using both simulations and observations, respectively. Colorbars show the μk_{CMB} units for each patch.

3. Methodology

An artificial neural network is a machine learning framework composed of computational nodes, known as neurons, which are structured into multiple layers. Each neuron contains a set of weights that are adjusted during the training process. As input data propagate through the network, a loss function is evaluated at the output layer. This loss is minimized to compute a gradient that updates all the weights across the network using backpropagation. Once this update is complete, the process repeats for a new training cycle, known as an epoch. This iterative learning process then constitutes an optimization problem.

Neural networks are particularly effective for image-related tasks, since image data can be represented as two-dimensional arrays. A common application is image segmentation (Long et al. 2015). In such cases, the learnable parameters are organized into matrices known as kernels. This kind of networks are then suitable for component separation processes, where the physical emissions present a high complexity and non-linearity. In this study, we adapt and extend the Cosmic Microwave Background Extraction Neural Network (CENN), initially introduced in Casas et al. (2022) to separate the CMB with respect to foregrounds in intensity maps, and then extended to polarization maps in Casas et al. (2023).

This network is a fully-convolutional one that builds upon the U-Net architecture (Ronneberger et al. 2015). It is designed to reconstruct clean microwave maps from noisy background data. The theoretical foundations of such architectures for multi-frequency image processing are covered in Goodfellow (2010), while the physical ones are described in detail in Appendix A. While those references provide comprehensive explanations, we include here a concise summary of the network's structure and functionality.

The network begins by ingesting the so-called Input Total patches, which contain sky maps at multiple frequencies. In this work, we aim to use QUIJOTE MFI data only, i.e. 11, 13, 17 and 19 GHz. This input data passes through six encoding blocks where convolutional filters are applied to extract features across various channels. An activation function introduces non-linearity to allow more complex patterns to be learned. After the encoding stage, the data passes through six decoding blocks, where deconvolutional operations reconstruct the signal. Each decoding block is linked to its corresponding encoder via skip connections, enabling the network to recover fine-grain details by comparing and integrating feature maps from both stages. The final layer outputs a patch representing the estimated map. This output is then used to compute the loss, which drives weight up-

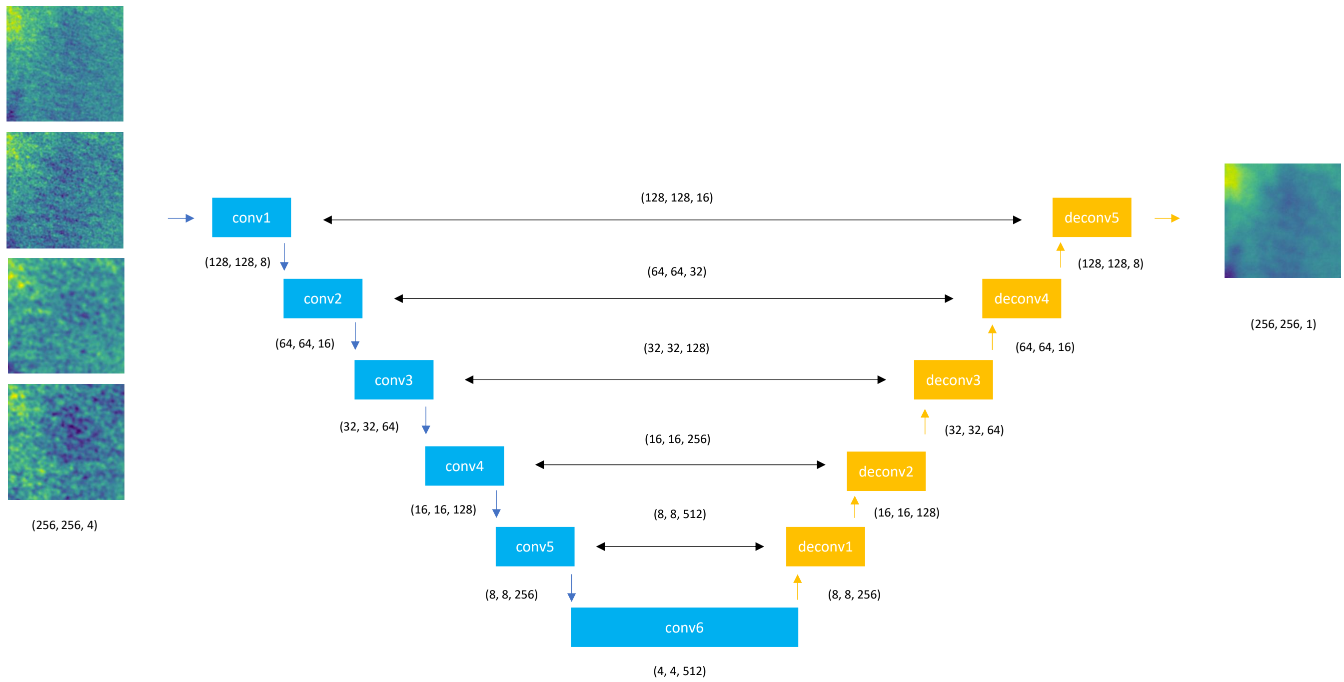

Fig. 3: Scheme of the architecture of the neural network used in this work. We show for visualization purposes the kind of input and output patches the network reads and outputs, respectively.

dates during training through gradient descent and backpropagation. The cycle then continues with the next epoch.

The full network architecture is depicted in Figure 3 and comprises six convolutional (encoder) blocks, each including convolution and pooling layers with kernel sizes of 9, 9, 7, 7, 5, and 3 pixels, and kernel counts of 8, 2, 4, 2, 2, and 2, respectively. These layers employ 8, 16, 64, 128, 256, and 512 filters and use a downsampling factor of 2. Padding type "Same" is applied throughout to preserve spatial dimensions. After that, six deconvolutional (decoder) blocks are connected and use similar deconvolution and pooling layers with kernel sizes of 3, 5, 7, 7, 9, and 9, and kernel counts of 2, 2, 2, 4, 2, and 8. The associated filter counts are 256, 128, 64, 16, 8, and 1. The same downsampling factor and padding strategy are used here, and all layers use the leaky ReLU activation function.

4. Results

4.1. Validation by simulations

We consider for validation a dataset formed by 100 simulations for each sky region. For each region, we take the patches centered at the positions listed in Table 2. The network then outputs 100 synchrotron Q and U patches at 11 GHz for each region. An example of an output patch is shown in Figure 2, where the output from the network is shown at the middle row and the left column, and the difference with respect input, i.e. the synchrotron s5 model, is displayed at the bottom row, middle column.

We then estimate the average EE and BB power spectra for each 100 region patches using NaMaster (Alonso et al. 2019), and we fit the data by assuming a power law model as described in (1), and following the parametrization defined in (2), for multipoles in the range $50 \lesssim l \lesssim 200$. The fitting is performed by using the curve fit method from Scipy (Jones et al. 2001). We then obtain estimates of the synchrotron amplitude A_S and the index α_S for both EE and BB, and then we can estimate the ratio of the amplitudes, $r = A_S^{BB}/A_S^{EE}$.

Figure 4 presents the comparison between the synchrotron α_S index in the input s5 simulations (in blue) with respect the estimates from the neural network (in red) at 11 GHz in the simulated QUIJOTE sky, for EE and BB in the left and right panels, respectively, and for each sky region. The index absolute error is shown in the bottom subpanel in black. The error bars for each estimation represent the 1σ standard deviation for the 100 simulations. The dashed horizontal lines represent the average estimates and the shaded areas display the 1σ standard deviation for these average values.

Overall, the neural network captures relatively well the spatial behavior of the index in EE, as well as the average one, although some biases are found in BB. Particularly, there is a strong bias for EE in Region 6, and several ones in BB, especially in Regions 8, 9, 19 and 20, suggesting localized reconstruction challenges, probably due to low signal-to-noise ratio (SNR, Regions 6, 8 and 9) and/or complex spatial structure (Regions 18 and 20).

In summary, the neural network demonstrates overall accuracy in recovering the polarized synchrotron index α_S, with better performance in the E-mode component. The localized biases identified in certain B-mode regions deserve further investigation and may point to Galactic areas where model refinement could improve generalization and robustness. Future trainings should use data at frequencies where synchrotron SNR is higher in some regions, as well as curvature data should be considered in parallel with no-curvature one.

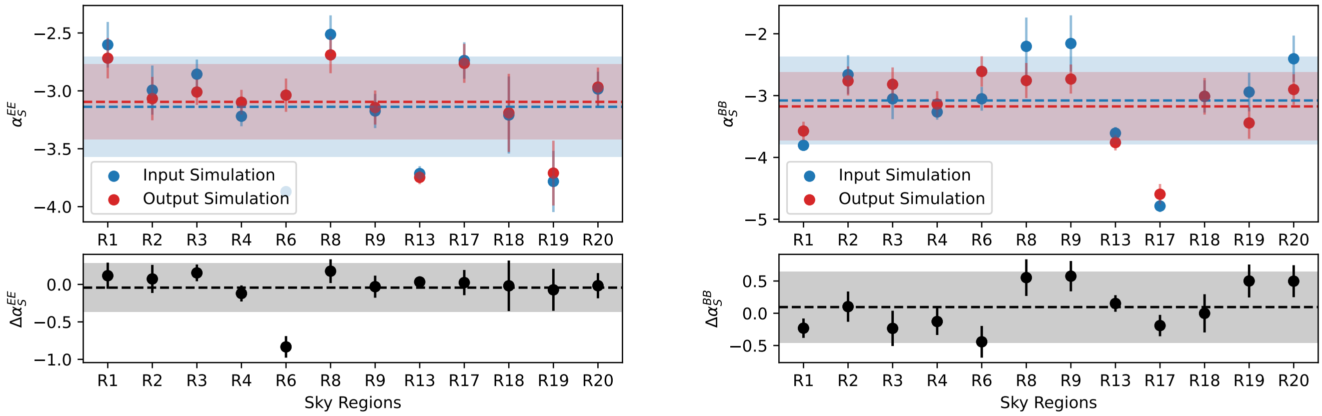

Fig. 4: Polarized synchrotron index α_S comparison at 11 GHz between the input s5 model (blue dots) and the outputs from the neural network (in red), after fitting both *EE* (left panel) and *BB* spectra (right panel) for each sky region, while bottom subpanel displays the absolute error between them. The average index is shown in both panels as a dashed blue and red lines, respectively. The average difference is represented as a dashed black line. The errorbars for each point show the 1σ uncertainty for each sky region evaluated over 100 simulations. Shaded colored areas show the 1σ uncertainties for each average value.

Figure 5 presents the comparison between the synchrotron A_S amplitude in the input s5 simulations (in blue) with respect the estimates from the neural network (in red) at 11 GHz in the simulated QUIJOTE sky, for *EE* and *BB* in the left and right panels, respectively, and for each sky region. The index absolute error is shown in the bottom subpanel in black. The error bars for each estimation represent the 1σ standard deviation for the 100 simulations. The dashed horizontal lines represent the average estimates and the shaded areas display the 1σ standard deviation for these average values.

As shown, in both polarization modes, the network outputs follow the overall trend of the last section, i.e. for *EE*, the estimated amplitudes are in general similar than the input ones, mainly due to the high SNR at 11 GHz in most of the regions for this mode. However, as in the last section, Region 6 remains the one with the higher discrepancies with respect to the input one, because the low SNR of this sky region. For *BB*, there are more estimates that present strong biases, especially regions with low SNR as R2, R6 and R9.

In summary, the neural network exhibits also for this quantity relatively robust performance in recovering the amplitude of polarized synchrotron emission in both *E* and *B*-mode components, but the SNR of the simulated instrument as well as the sky signal in some sky regions make it difficult some estimations, especially for *BB*. As for the synchrotron index estimation, the accuracy of this estimation would likely improve with the addition of training data with higher quality which consider all the possible physical properties of polarized synchrotron emission. This will be evaluated in a future work.

Finally, Figure 6 shows the comparison between the synchrotron *BB* and *EE* amplitude ratio in the input simulations (in blue) with respect to the ratio from the outputs of the neural network (in red). Their absolute difference is shown in the bottom subpanel in black for each sky region. The errorbars for each estimation show the 1σ uncertainty by propagating the errors from the 100 simulations using

$$\delta r = r \cdot \sqrt{\left(\frac{\delta A_{BB}}{A_{BB}}\right)^2 + \left(\frac{\delta A_{EE}}{A_{EE}}\right)^2}, \tag{3}$$

where δr is the uncertainty in r, δA_{XX} is the uncertainty in the amplitudes and A_{XX} are the amplitudes.

The dashed horizontal line represents the mean A_S^{BB}/A_S^{EE} ratios, averaged from all the regions (and assumed to be the one at all sky) and then the shaded areas presents the 1σ uncertainties of these values.

Overall, the neural network seems to successfully reconstruct the ratio with good agreement to the input simulations in most sky regions. The predicted values closely follow the input distribution, with the majority of the points lying within the uncertainty range. The mean of the output values remains consistent with that of the input, suggesting that the model captures the global behavior of the synchrotron polarization ratio, although some regions such R6 display an unconsistent value between input and output. These discrepancies may stem from the intrinsic variability and low signal-to-noise ratio of the synchrotron *B*-mode component, which is more challenging to accurately model.

In summary, the network demonstrates a strong ability to reconstruct the synchrotron polarization amplitude ratio across different sky regions, although bias, that should carefully consider appear in low SNR regions.

4.2. Application to real QUIJOTE MFI data

Once we deduce that the results obtained by the neural network are generally consistent with the input simulations, we decide to test its performance on the QUIJOTE MFI real observations, publicly available. An example of the input and output patches of the QUIJOTE MFI observations for the North Polar Spur (Region 13) at 11 GHz are shown in Figure 2, being the input sky represented at the top row, middle column and the output from the network shown at the middle row and column. Also the difference with respect the synchrotron s5 model is plotted at the bottom row, right column. Moreover, we show in the middle row and right column the difference between the output from the network and the simulations at the same point in the sky. For completeness, the same but for the input sky is displayed in the top row, right column.

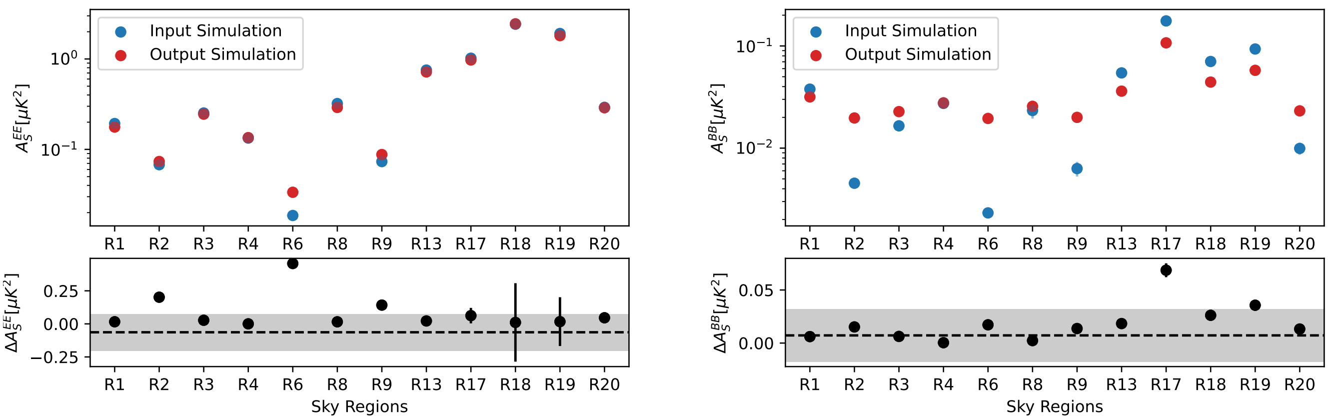

Fig. 5: Polarized synchrotron amplitude A_S comparison at 11 GHz in logarithmic scale between the input s5 model (blue dots) and the outputs from the neural network (in red), after fitting both EE (left panel) and BB spectra (right panel) for each sky region, while bottom subpanel displays in linear scale the absolute error between them. The average difference is represented as a dashed black line. The errorbars for each point show the 1σ uncertainty for each sky region evaluated over 100 simulations. Shaded colored area show the 1σ uncertainty for the absolute error average value.

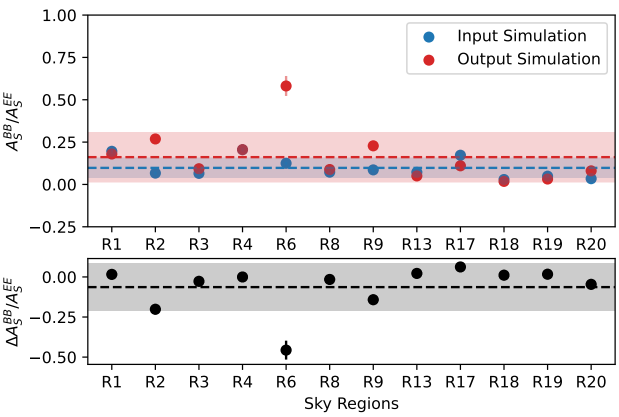

Fig. 6: Polarized synchrotron ratio comparison between B and E amplitudes at 11 GHz between the input s5 model (blue dots) and the outputs from the neural network (in red), after fitting both spectra for each sky region. The bottom subpanel displays the absolute error between them. The average ratio is shown as a dashed blue and red lines, respectively. Shaded colored areas show the 1σ respective uncertainties. The average difference is represented as a dashed black line. The errorbars for each point show the 1σ uncertainty for each sky region propagated from A_S^{BB} and A_S^{EE} uncertainties using equation 3 evaluated over 100 simulations. Shaded colored area show the 1σ uncertainty for the absolute error average value.

The main insights extracted from this particular example is that it seems to be a difference at the middle scales between the synchrotron s5 model and the QUIJOTE MFI observations, which are probably synchrotron structures not properly modeled. Moreover, once the network is trained, after comparing the difference between its outputs from the simulations and the observations, it seems that it is capable of generalize to different data since at the bottom row and middle column of Figure 2, the network is mainly recovering the synchrotron emission with some residual instrumental noise, while for the observations it is recovering such synchrotron structures that were not in the training nor validating data.

We then estimate both EE and BB spectra over each one of the 12 sky patches to estimate the synchrotron parameters at 11 GHz in the same way as for simulations. We plot their average value from all regions in Figure 7 at the left and right panels, respectively, in comparison with respect to the average power spectra of the QUIJOTE MFI sky (i.e. sky signal plus instrumental noise), which is some orders of magnitude higher at middle scales due mainly to instrumental noise. As shown, the spectra presents in both cases a power-law shape, which is more clear for EE due to its higher SNR with respect to BB. Therefore, no curvature signals seem to be visually present in this work and the addition of more data from higher frequencies (WMAP and *Planck*) and lower ones (CBASS) becomes mandatory for such analysis.

Based on the average spectra, we then fit it individually for each sky region by assuming a power-law behavior by following equation 1. Results are summarize in Table 2, and represented in Figures 8, 9 and 10.

In particular, Figure 8 presents our estimations for the synchrotron α_S index in the QUIJOTE real observations at 11 GHz after fitting both EE (left panel) and BB-mode spectra (right panel) with the same conditions than the ones described in Section 4.1 with the simulations, and for each sky region. The errorbars for each estimation show the statistical+systematical uncertainty, where the statistical is the one from the 100 simulations on each regions presented in the last section and the systematical is the bias between input s5 and output also showed in the last section for the same simulations.

Moreover, the dashed horizontal line represents the mean estimated synchrotron index, averaged from all the regions (and assumed to be the one at all sky), in comparison with respect to previous similar analyses (Rubiño-Martín et al. (2023) (black dashed line), Martire et al. (2022) (red dashed line) and Planck Collaboration et al. (2020b) (yellow dashed line)). Shaded areas show the 1σ uncertainty for each average value, being in our case the sum of statistical and systematical uncertainty value for this average. We did not compare with Krachmalnicoff et al. (2018) because of their different sky coverage with respect to ours, al-

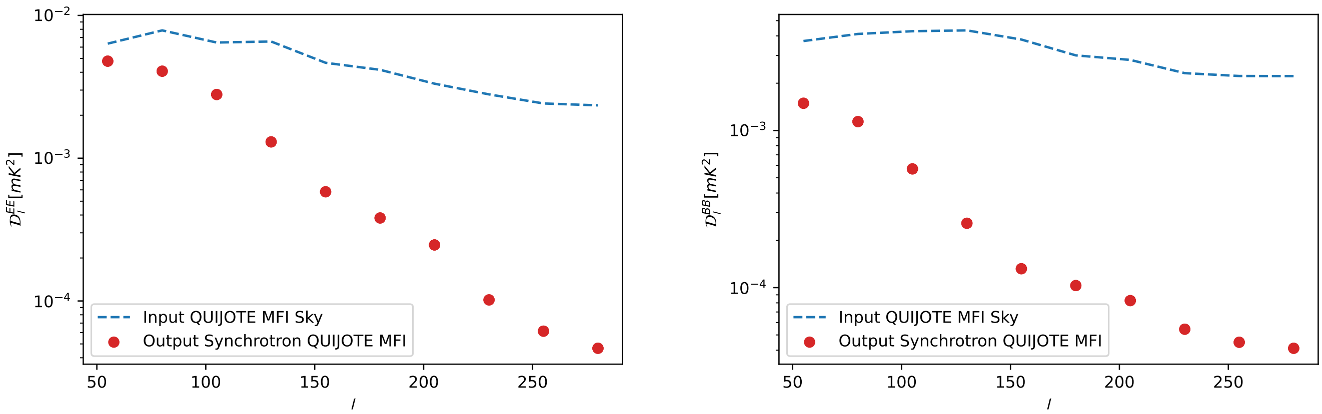

Fig. 7: Power spectra comparison at 11 GHz between the output synchrotron averaged over all the 12 sky regions (in red dots) with respect to the power spectra of the QUIJOTE MFI sky (in blue dashed line) for EE (left panel) and BB (right panel).

Table 2: Summary of our synchrotron estimates in the QUIJOTE MFI observations at 11 GHz for each sky region. From left to right, columns show: the sky region analyzed, for which patch central position is displayed in Table 1, the estimated amplitudes A_S^{EE} and A_S^{BB}, the indeces α_S^{EE} and α_S^{BB}, and finally the ratio between the amplitudes A_S^{BB}/A_S^{EE}. The data show on each row both the statistical and systematical uncertainties, respectively, also averaged for the Galactic Plane regions (GP), high-latitudes regions (HGL) and all regions, as defined in 1.

Región	$A_S^{EE}[\mu k^2]$	$A_S^{BB}[\mu k^2]$	α_S^{EE}	α_S^{BB}	A_S^{BB}/A_S^{EE}
1	0.32 ± 0.01 ± 0.02	0.14 ± 0.01 ± 0.01	-2.86 ± 0.17 ± 0.12	-3.13 ± 0.15 ± 0.23	0.44 ± 0.01 ± 0.02
2	0.24 ± 0.01 ± 0.01	0.06 ± 0.002 ± 0.02	-2.7 ± 0.2 ± 0.07	-4.1 ± 0.2 ± 0.1	0.25 ± 0.03 ± 0.20
3	0.53 ± 0.01 ± 0.01	0.07 ± 0.01 ± 0.01	-2.86 ± 0.11 ± 0.15	-1.9 ± 0.3 ± 0.2	0.14 ± 0.01 ± 0.03
4	0.54 ± 0.01 ± 0.002	0.20 ± 0.01 ± 0.000	-3.5 ± 0.1 ± 0.1	-3.8 ± 0.2 ± 0.1	0.36 ± 0.02 ± 0.003
6	0.21 ± 0.002 ± 0.02	0.12 ± 0.01 ± 0.02	-3.3 ± 0.1 ± 0.8	-2.3 ± 0.3 ± 0.4	0.50 ± 0.06 ± 0.46
8	0.46 ± 0.02 ± 0.03	0.10 ± 0.01 ± 0.002	-2.83 ± 0.16 ± 0.18	-2.8 ± 0.3 ± 0.5	0.21 ± 0.01 ± 0.02
9	0.25 ± 0.01 ± 0.01	0.10 ± 0.01 ± 0.01	-3.17 ± 0.15 ± 0.03	-3.1 ± 0.2 ± 0.6	0.46 ± 0.02 ± 0.14
13	2.50 ± 0.01 ± 0.03	0.10 ± 0.002 ± 0.02	-3.00 ± 0.06 ± 0.02	-2.71 ± 0.10 ± 0.15	0.04 ± 0.02 ± 0.02
17	11.9 ± 0.1 ± 0.1	4.60 ± 0.01 ± 0.07	-2.77 ± 0.17 ± 0.03	-2.82 ± 0.17 ± 0.19	0.39 ± 0.01 ± 0.06
18	11.1 ± 0.3 ± 0.02	5.10 ± 0.01 ± 0.03	-2.39 ± 0.34 ± 0.02	-3.50 ± 0.30 ± 0.01	0.46 ± 0.01 ± 0.01
19	7.6 ± 0.2 ± 0.1	0.36 ± 0.01 ± 0.04	-3.36 ± 0.28 ± 0.07	-3.18 ± 0.26 ± 0.50	0.05 ± 0.01 ± 0.02
20	4.17 ± 0.02 ± 0.01	0.21 ± 0.01 ± 0.01	-3.55 ± 0.17 ± 0.02	-2.61 ± 0.25 ± 0.50	0.05 ± 0.01 ± 0.05
GP	7.60 ± 0.20 ± 0.03	1.88 ± 0.01 ± 0.03	-3.10 ± 0.30 ± 0.02	-3.10 ± 0.20 ± 0.20	0.18 ± 0.01 ± 0.01
HGL	0.63 ± 0.01 ± 0.07	0.11 ± 0.01 ± 0.004	-3.05 ± 0.15 ± 0.05	-2.98 ± 0.23 ± 0.04	0.30 ± 0.02 ± 0.10
All	3.31 ± 0.07 ± 0.01	0.93 ± 0.01 ± 0.01	-3.04 ± 0.17 ± 0.04	-3.00 ± 0.24 ± 0.10	0.28 ± 0.02 ± 0.06

though as described in Section 1, we found compatible average results.

The estimated average values of the synchrotron indeces are $\alpha_S^{EE} = -3.04 \pm 0.21$ and $\alpha_S^{BB} = -3.00 \pm 0.34$, consistent with all the previous analyses, especially with the one using the same data (Rubiño-Martín et al. 2023), which found $\alpha_S^{EE} = -3.00 \pm 0.16$ and $\alpha_S^{BB} = -3.08 \pm 0.42$ for a Galactic mask of $|b| > 5°$.

Furthermore, the index shows a clear spatial variability along the sky with some of the regions showing a flatter index while others presenting a steeper one. There are also regions showing high discrepancies between α_S^{EE} and α_S^{BB}, some of them indeed inside the errorbars, thus we can infer that some biases from training the network with a simplistic synchrotron model and/or noise, and other ones outside the errorbars (R2, R3, R18), that we relate to either structures not reconstructed in the B-mode (R18) and/or low SNR regions (R2 and R3). Also, possible curvature in the data, especially in the regions with higher SNR as so the Galactic plane, could explain these discrepancies since we did not include any curvature in the training and validating data.

Moreover, Figure 9 displays our estimates for the synchrotron A_S amplitude in the QUIJOTE MFI real observations at 11 GHz, after fitting both EE (left panel) and BB-mode spectra (right panel), and for each sky region. The errorbars for each estimation show the statistical+systematical uncertainty, calculated as in the previous analysis.

We estimate average amplitudes considering all the sky regions of $A_S^{EE} = 3.31 \pm 0.08\mu K^2$ and $A_S^{BB} = 0.93 \pm 0.02\mu K^2$, considering both statistical and systematical uncertainties, estimated as in the previous section. In the Galactic Plane, we find $A_S^{EE} = 7.60 \pm 0.23\mu K^2$ and $A_S^{BB} = 1.88 \pm 0.04\mu K^2$ and in the outer regions $A_S^{EE} = 0.63 \pm 0.08\mu K^2$ and $A_S^{BB} = 0.11 \pm 0.014\mu K^2$.

Our estimates, indeed, are also close to the Rubiño-Martín et al. (2023) ones if we compare their Galactic cuts with ours (an average $A_S^{EE} = 1.52 \pm 0.15\mu K^2$ and $A_S^{BB} = 0.52 \pm 0.15\mu K^2$ for $|b| > 5°$, and $A_S^{EE} = 0.81 \pm 0.19\mu K^2$ and $A_S^{BB} = 0.18 \pm 0.13\mu K^2$ for $|b| > 20°$).

Although the estimates follow the expected behavior, i.e. regions with low SNR would present the lower amplitudes and the same for the high SNR regions, it seems to be an overestimation

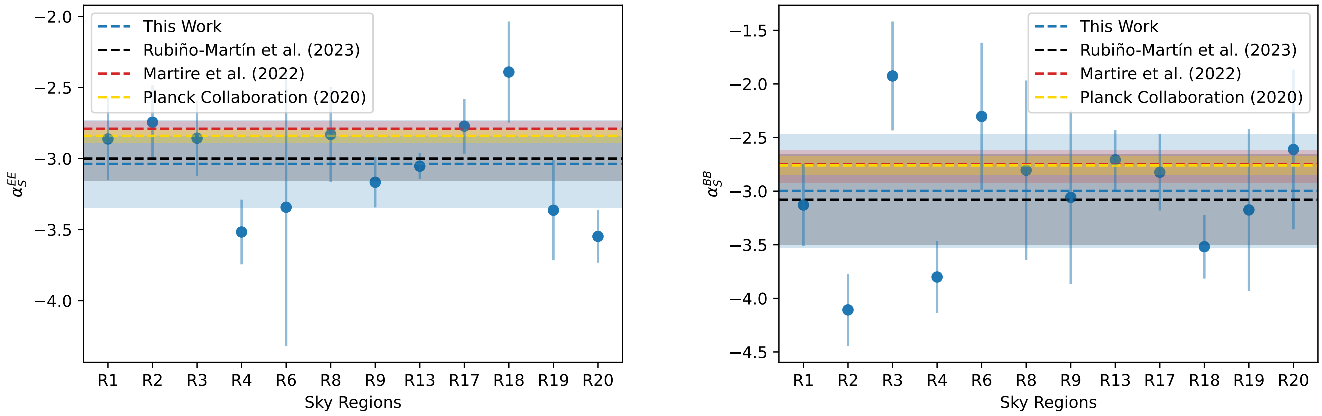

Fig. 8: Polarized synchrotron index α_S estimates (blue dots) in the QUIJOTE MFI observations at 11 GHz by fitting *EE* (left panel) and *BB* spectra (right panel) for each sky region. The average index is shown in both panels as a dashed blue line. The errorbars for each point represents both the statistical and systematical uncertainties for each sky region. As a reference, we show the comparison with Rubiño-Martín et al. (2023) (black dashed line), Martire et al. (2022) (red dashed line) and Planck Collaboration et al. (2020b) (yellow dashed line) at similar sky mask coverages than in this work. Shaded colored areas display the respective 1σ uncertainties for every average estimation.

of the Galactic region amplitudes since R13 appears to be lower than theirs, and should be as known the region with the highest SNR. This overestimation is likely due to residual instrumental noise in the maps, and therefore it is expected to have more accurate estimates either joining data from other surveys and/or with future observations with higher sensitivity as QUIJOTE MFI2 ones.

Finally, Figure 10 shows our estimates for the ratio between B and E amplitudes in the QUIJOTE MFI real observations at 11 GHz. The errorbars for each estimation show the statistical+systematical uncertainty. The statistical one have been estimated by propagating the errors from the ratio A_S^{BB}/A_S^{EE} in the simulations. The systematic one is given by the bias between input and output ratio in the simulations.

The dashed horizontal line represents the average A_S^{BB}/A_S^{EE} ratio from all the regions (and assumed to be the one at all sky). As a comparison, we show the results from previous analyses, Rubiño-Martín et al. (2023) (in a black dashed line), Martire et al. (2022) (in a red dashed line) and Planck Collaboration et al. (2020b) (in a yellow dashed line). Shaded areas show the 1σ uncertainty for each average value.

We find an average ratio of 0.28 ± 0.08, which is closer to the Rubiño-Martín et al. (2023) one (0.34 ± 0.1 for $|b| > 5°$). Also, we can compare with other analyses such Planck Collaboration et al. (2020b) (≈ 0.39), Martire et al. (2022) (≈ 0.22), although they used data at higher frequencies. As shown, our value is also consistent with them but they had lower uncertainty, likely due to the combination of *Planck* and WMAP data instead of using QUIJOTE data only.

As in the previous sections, low SNR regions such R2, R6 and R9 present the highest uncertainties, as expected, due to the error propagation from A_S^{BB} and A_S^{EE}.

5. Discussion and conclusions

In this work, we aimed to analyze the spatial variation of polarized synchrotron emission in the QUIJOTE MFI data by fitting both *EE* and *BB* spectra on output maps from a novel component separation technique called CENN, presented firstly in Casas et al. (2022) with intensity maps, and then extended to polarization ones in Casas et al. (2023).

As said before, our analysis aims to extract reliable estimates of synchrotron parameters, such as the synchrotron index α_S and the amplitude for both E and B-modes, as so as the ratio between B and E amplitudes. The spatial variability will be studied by considering several physically distinct sky regions, defined in Fuskeland et al. (2014). The reason to use QUIJOTE data only without making joint analyses with other experiments is manly motivated by the idea to firstly evaluate the ability of this kind of models when dealing with real data instead of simulations (which is in fact mainly the type of training and validating data used for evaluating the performance of this kind of models in the literature), before implementing the model with joint data from more experiments, such WMAP, Planck and/or CBASS, which would be investigated in a future work.

To train and validate the neural network, we have constructed a set of realistic simulations that incorporate all the elements forming the microwave sky at the frequencies covered by the QUIJOTE MFI instrument, i.e. synchrotron, dust, AME, the CMB and radio point sources, and also we added instrumental noise following the sensitivity specifications of the QUIJOTE MFI instrument, but without taking into account systematic effects, although we know that this could be a simplification with respect the real data in polarization, but we did not want to make a complex training in this first analysis. Synchrotron emission was modeled with the s5 PySM configuration, which assumes a spatial variability in the spectral index between the Galactic plane and the extragalactic regions, and also incorporates small scale features. We have not used a curvature method in order to not giving prior information about this kind of behavior in the training process, to consider the possibility of finding some insights of curvature in the QUIJOTE observations after validating the network.

The simulations were cut into square patches of 256×256 pixels at the QUIJOTE's angular resolution (approximately 414 arcseconds per pixel), covering the four MFI frequencies of 11, 13, 17, and 19 GHz. Each sky region was populated with 100 independent simulations, allowing for robust uncertainty estima-

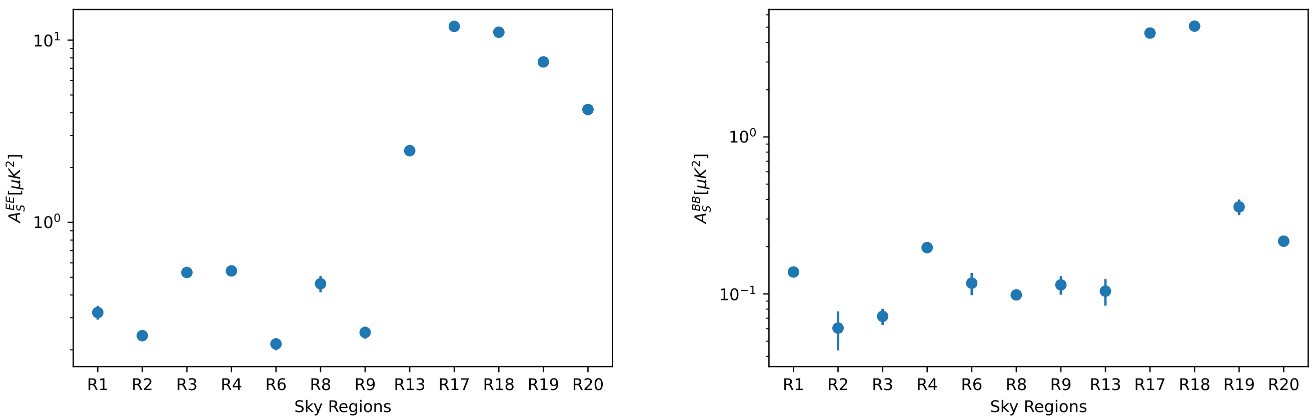

Fig. 9: Polarized synchrotron amplitude A_S estimates in logarithmic scale in the QUIJOTE MFI observations at 11 GHz after fitting *EE* (left panel) and *BB* spectra (right panel) for each sky region. The errorbars for each point represents both the statistical and systematical uncertainties for each sky region.

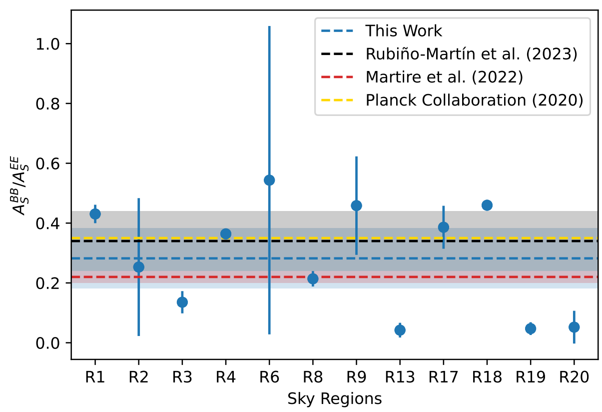

Fig. 10: Polarized synchrotron estimates for the ratio between A_S^{BB} and A_S^{EE} amplitudes (blue dots) in the QUIJOTE MFI observations at 11 GHz for each sky region. The errorbars for each point show both statistical and systematical uncertainties for each sky region propagated from A_S^{BB} and A_S^{EE} uncertainties using equation 3. The average ratio is displayed as a dashed blue line. As a reference, we show the comparison with Planck Collaboration et al. (2020b) (yellow dashed line), Martire et al. (2022) (red dashed line) and Rubiño-Martín et al. (2023) (black dashed line) at similar sky mask coverages than in this work. Shaded colored areas display the respective 1σ uncertainties for every average estimation.

tion. For the observational analysis, we employed the publicly available QUIJOTE MFI maps, extracting one patch per region, centered on the same positions used in the simulations.

After being trained with patches at random positions in the sky, the neural network demonstrated strong performance when recovering the synchrotron signal from simulated sky patches, mainly found an accurate recovery of the synchrotron index for both polarization modes, with average absolute errors below 0.5 in most of the sky regions, and generally better performance for E compared to the B-mode. We also found a robust estimation of the synchrotron amplitude, even in regions with low signal-to-noise ratios, with small deviations appearing primarily in B-mode measurements, and a consistent recovery of the amplitude ratio, in agreement with theoretical expectations and simulation inputs. However, as shown, the results for the B-mode still present some variations with respect to the input ones, as expected, since the signal is fainter than the E one, and more sensitive to instrumental noise.

Once validated on realistic simulations, the network was applied to real QUIJOTE MFI data. Despite being trained exclusively on synthetic maps, the network successfully extracted meaningful synchrotron structures from real sky observations. In fact, the output maps revealed mid-scale features not present in the training data, suggesting that the neural network can generalize to Interstellar medium complexities. Moreover, we found clear discrepancies for the synchrotron index and a systematic overestimation of the amplitude with respect simulations (although input and output simulations closely matched together) in regions with a strong emission, that we interpret as an incorrect modeling of the synchrotron emission, or also possible curvature in the data. This will be further investigated in future works.

The average values from all the regions are in general consistent with previous analyses. We found $\alpha_S^E = -3.04 \pm 0.21$ and $\alpha_S^B = -3.00 \pm 0.4$, amplitudes of $A_S^E = 3.31 \pm 0.08 \mu K^2$ and $A_S^B = 0.93 \pm 0.02 \mu K^2$, and a ratio between B and E amplitudes of $A_S^B/A_S^E = 0.28 \pm 0.08$, considering systematic+statistical uncertainties in all the cases.

We also found notable spatial variations in the synchrotron properties output by the network, as previous analyses found for other microwave experiments and frequencies. In particular, we estimate that, at high Galactic latitudes (R1-R13), synchrotron generally exhibited flatter indices, with average values of $\alpha_S^E = -3.05 \pm 0.2$ and $\alpha_S^B = -2.98 \pm 0.27$, lower amplitudes ($A_S^E = 0.63 \pm 0.08 \mu K^2$ and $A_S^B = 0.11 \pm 0.01 \mu K^2$), and higher B to E amplitude ratios ($A_S^B/A_S^E = 0.3 \pm 0.12$). On the other hand, Galactic plane regions (R17–R20) showed steeper indices , with average values of $\alpha_S^E = -3.10 \pm 0.32$ and $\alpha_S^B = -3.1 \pm 0.4$, higher amplitudes ($A_S^E = 7.60 \pm 0.23 \mu K^2$ and $A_S^B = 1.88 \pm 0.04 \mu K^2$), and lower B to E amplitude ratios ($A_S^B/A_S^E = 0.18 \pm 0.02$), indicating strong E-mode dominance, as expected.

In conclusion, as we know, the physical behavior of the Interstellar Medium is extremely complex in polarization at these frequencies. Then, overall, this work is a huge step on the validation of these methods for their use in cosmic microwave background present and future data. We have presented a methodology which can be used for foreground cleaning and separation, in order to construct foreground templates to help to optimize component separation methods before future observations, as so as, with the properly data and simulations, it could be used also as a complementary component separation method itself with respect parametric and semi-blinds ones in order to give robust estimates with different kind of methodologies.

Future work, as said before, will focus on extending this approach by incorporating additional data from WMAP, Planck LFI, and/or upcoming survey data as CBASS, as so as improving the foreground and instrumental noise modeling. This will enhance the robustness of the network across a broader frequency range, improve performance in low signal regions, and help to mitigate systematic uncertainties.

Acknowledgements. JMC, LB and JGN acknowledge the CNS2022-135748 / MCIN/AEI/10.13039/501100011033 project. JMC, LB, JGN, DC, RFF and JAC acknowledge the PID2021-125630NB-I00 / MCIN/AEI/10.13039/501100011033 project. JARM and RGS acknowledge the PID2023-151567NB-I00 project. JMC, JARB, RTGS and RBB acknowledge both PID2023-151567NB-I00 / 10.13039/501100011033 and RadioForegroundsPlus HORIZON-CL4-2023-SPACE-01 / GA 101135036 projects.
The authors would like to faithfully thank the COSMOGLOBE Collaboration for making publicly available the sky map divided in regions that we used along this work.
This research has made use of the packages `Matplotlib` (Hunter 2007), `Keras` (Chollet 2015), `Numpy` (Oliphant 2006), `Namaster` (Alonso et al. 2019), `HEALPix` (Górski et al. 2005) and `Healpy` (Zonca et al. 2019) packages.

References

Alonso, D., Sanchez, J., Slosar, A., & LSST Dark Energy Science Collaboration. 2019, MNRAS, 484, 4127
Bonavera, L., González-Nuevo, J., Argüeso, F., & Toffolatti, L. 2017, MNRAS, 469, 2401
Casas, J. M., Bonavera, L., González-Nuevo, J., et al. 2022, A&A, 666, A89
Casas, J. M., Bonavera, L., González-Nuevo, J., et al. 2023, Recovering the E and B-mode CMB polarization at sub-degree scales with neural networks
Chollet, F. 2015, Keras, https://github.com/fchollet/keras
de la Hoz, E., Barreiro, R. B., Vielva, P., et al. 2023, MNRAS, 519, 3504
Draine, B. T. 2011, Physics of the Interstellar and Intergalactic Medium
Duchi, J., Hazan, E., & Singer, Y. 2011, J. Mach. Learn. Res., 12, 2121–2159
Eriksen, H. K., Dickinson, C., Lawrence, C. R., et al. 2006, New A Rev., 50, 861
Eriksen, H. K., Jewell, J. B., Dickinson, C., et al. 2008, ApJ, 676, 10
Fuskeland, U., Andersen, K. J., Aurlien, R., et al. 2021, A&A, 646, A69
Fuskeland, U., Wehus, I. K., Eriksen, H. K., & Næss, S. K. 2014, ApJ, 790, 104
Génova-Santos, R., Rubiño-Martín, J. A., Rebolo, R., et al. 2015, in Highlights of Spanish Astrophysics VIII, ed. A. J. Cenarro, F. Figueras, C. Hernández-Monteagudo, J. Trujillo Bueno, & L. Valdivielso, 207–212
Gold, B., Odegard, N., Weiland, J. L., et al. 2011, ApJS, 192, 15
González-Nuevo, J., Toffolatti, L., & Argüeso, F. 2005, ApJ, 621, 1
Goodfellow, I. J. 2010, Technical Report: Multidimensional, Downsampled Convolution for Autoencoders, Tech. rep., Université de Montréal
Goodfellow, I. J., Bengio, Y., & Courville, A. 2016, Deep Learning (Cambridge, MA, USA: MIT Press), http://www.deeplearningbook.org
Górski, K. M., Hivon, E., Banday, A. J., et al. 2005, ApJ, 622, 759
Hensley, B. S. & Draine, B. T. 2021, ApJ, 906, 73
Hoyland, R. J., Rubiño-Martín, J. A., Aguiar-Gonzalez, M., et al. 2022, in Society of Photo-Optical Instrumentation Engineers (SPIE) Conference Series, Vol. 12190, Millimeter, Submillimeter, and Far-Infrared Detectors and Instrumentation for Astronomy XI, ed. J. Zmuidzinas & J.-R. Gao, 1219033
Hunter, J. D. 2007, Computing In Science & Engineering, 9, 90
Jones, E., Oliphant, T., Peterson, P., et al. 2001, SciPy: Open source scientific tools for Python
Krachmalnicoff, N., Carretti, E., Baccigalupi, C., et al. 2018, A&A, 618, A166
Lecun, Y., Bottou, L., Bengio, Y., & Haffner, P. 1998, Proceedings of the IEEE, 86, 2278
Long, J., Shelhamer, E., & Darrell, T. 2015, in Proceedings of the IEEE conference on computer vision and pattern recognition, 3431–3440
Martire, F. A., Barreiro, R. B., & Martínez-González, E. 2022, J. Cosmology Astropart. Phys., 2022, 003
Oliphant, T. 2006, NumPy: A guide to NumPy, USA: Trelgol Publishing, [Online; accessed <today>]
Page, L., Hinshaw, G., Komatsu, E., et al. 2007, ApJS, 170, 335
Planck Collaboration, Abergel, A., Ade, P. A. R., et al. 2014, A&A, 571, A11
Planck Collaboration, Ade, P. A. R., Aghanim, N., et al. 2015, A&A, 576, A104
Planck Collaboration, Aghanim, N., Akrami, Y., et al. 2020a, A&A, 641, A1
Planck Collaboration, Akrami, Y., Ashdown, M., et al. 2020b, A&A, 641, A4
Ronneberger, O., Fischer, P., & Brox, T. 2015, Medical Image Computing and Computer-Assisted Intervention – MICCAI 2015
Rubiño-Martín, J. A., Guidi, F., Génova-Santos, R. T., et al. 2023, MNRAS, 519, 3383
Rumelhart, D. E., Hinton, G. E., & Williams, R. J. 1986, Nature, 323, 533
The Pan-Experiment Galactic Science Group. 2025, arXiv e-prints, arXiv:2502.20452
Thorne, B., Dunkley, J., Alonso, D., & Næss, S. 2017, MNRAS, 469, 2821
Tucci, M., Toffolatti, L., de Zotti, G., & Martínez-González, E. 2011, A&A, 533, A57
Watts, D. J., Fuskeland, U., Aurlien, R., et al. 2024, A&A, 686, A297
Weiland, J. L., Addison, G. E., Bennett, C. L., Halpern, M., & Hinshaw, G. 2022, ApJ, 936, 24
Zonca, A., Singer, L. P., Lenz, D., et al. 2019, Journal of Open Source Software, 4, 1298

Appendix A: Model

On one side, our approach is grounded in the physical principles described in Eriksen et al. (2006) and Eriksen et al. (2008). On the other side, it adheres to the theoretical framework of CNNs and FCNs, as detailed in Rumelhart et al. (1986), Lecun et al. 1998, and Goodfellow et al. (2016).

Our model operates on patches x_ν of the microwave sky at various frequencies ν (specifically 143, 217, and 353 GHz), each modeled as a linear mixture of c astrophysical sources. These sources are represented by emission maps e_ν, convolved with the experiment's instrumental beam i_ν and superimposed with instrumental noise n_ν:

$$x_\nu = i_\nu * e_\nu + n_\nu, \tag{A.1}$$

where $*$ denotes convolution. The emission maps are composed as a linear combination of foreground components, each with distinct spectral properties:

$$e_\nu = \sum_c A_{c,\nu}\, s_c, \tag{A.2}$$

with A denoting the mixing matrix and s representing the set of component maps. Substituting into Equation (A.1), the full model becomes:

$$x_\nu = i_\nu * \left(\sum_c A_{c,\nu}\, s_c\right) + n_\nu. \tag{A.3}$$

Initially, all model parameters are randomly set. The neural network ingests a tensor of shape $N_{\text{pix}} \times N_{\text{pix}} \times N_\nu$, where $N_{\text{pix}} = 256$ and N_ν denotes the number of frequency channels. Spectral features are captured via multidimensional strided convolutions (Goodfellow 2010):

$$H_{\nu,i,j} = \sum_{k,m} W_{k,m,i}\, V_{s\circ\nu+k,m,j}, \tag{A.4}$$

where H are the hidden units, V are the input values, and W is the convolutional kernel. The operator s represents the stride vector, and $\circ$ indicates element-wise multiplication.

Subsequent convolutional blocks apply similar operations, utilizing outputs from previous layers as inputs.

In the decoder (deconvolutional blocks), we perform a strided transposed convolution across spectral dimensions:

$$R_{q,m,j} = \sum_{\nu,k\,|\,s\circ\nu+k=q}\ \sum_i W_{k,m,i}\, H_{\nu,i,j}, \tag{A.5}$$

where R denotes the deconvolved output, and H the activations from the previous layer. The condition after the vertical bar applies a modulo constraint.

Kernels W across all convolutional and deconvolutional layers are updated each epoch via minimization of the mean-squared error:

$$MSE = \frac{1}{2}\left|y - y'\right|^2, \tag{A.6}$$

where y is the predicted output and y' is the target (i.e., the true CMB map). The computed loss is then backpropagated to update layer parameters.

In the final deconvolutional layer, all spectral data is projected into a single channel, producing a reconstructed map at reference frequency $\nu_0 = 217$ GHz:

$$\tilde{x}_{\nu_0} = i_{\nu_0} * e_{\text{CMB},\nu_0} + \tilde{n}, \tag{A.7}$$

where $\tilde{n}$ represents deconvolution-induced noise, and e_{CMB,ν_0} is the CMB component.

Model parameters are updated each epoch according to:

$$\theta_{t+1} = \theta_t + \Delta\theta_t, \tag{A.8}$$

with the update step defined as:

$$\Delta\theta_t = -\alpha\, g_t, \tag{A.9}$$

where g_t is the gradient and α the learning rate, which is computed via the AdaGrad algorithm (Duchi et al. 2011):

$$\alpha = \frac{\eta}{\sqrt{G_t + \epsilon}}, \tag{A.10}$$

with G_t being the accumulated squared gradients, ϵ a stability term, and $\eta = 0.05$.

Upon propagating all minibatches through the network, the final gradient is computed at the last deconvolutional block as:

$$g_t = \frac{\partial E}{\partial O_{\nu_0}} = \frac{\partial}{\partial O_{\nu_0}}\left(\frac{1}{2}|O_{\nu_0} - l_{\nu_0}|^2\right) = |O_{\nu_0} - l_{\nu_0}|, \tag{A.11}$$

where l_{ν_0} is the ground truth label (CMB signal).

Backpropagation then proceeds by applying the chain rule. For the previous deconvolutional layer:

$$\begin{aligned} g_{t,W} &= \frac{\partial O_{\nu_0,LD}}{\partial W_{LD-1}} = \frac{\partial O_{\nu_0,LD}}{\partial O_{LD-1}} \cdot \frac{\partial O_{LD-1}}{\partial W_{LD-1}} \\ &= g_{t,LD} \cdot f_{LD-1}, \end{aligned} \tag{A.12}$$

$$\begin{aligned} g_{t,f} &= \frac{\partial O_{\nu_0,LD}}{\partial f_{LD-1}} = \frac{\partial O_{\nu_0,LD}}{\partial O_{LD-1}} \cdot \frac{\partial O_{LD-1}}{\partial f_{LD-1}} \\ &= g_{t,LD} \cdot W_{LD-1}, \end{aligned} \tag{A.13}$$

where $g_{t,W}$ and $g_{t,f}$ are the gradients with respect to weights and filters. These are derived using the 2D convolution formula:

$$O_{i,j} = \sum_{m=0}^{M}\sum_{n=0}^{N} f(i-m, j-n)\, W(m,n). \tag{A.14}$$

Here, LD and LD−1 stand for the last and penultimate deconvolutional blocks. This approach is similarly applied to prior deconvolutional layers.

Analogously, convolutional layers use:

$$g_{t,W} = g_{t,FD} \cdot f_{LC}, \tag{A.15}$$

$$g_{t,f} = g_{t,FD} \cdot W_{LC}, \tag{A.16}$$

where FD and LC refer to the first deconvolutional and last convolutional blocks, respectively. All other convolutional blocks follow the same gradient-based update rules.

Appendix B: Full sky maps

In this appendix, we aim to show the same results than the ones presented in Section 4, but displayed in full-sky maps and divided by the analyzed sky regions. Figure B.1 shows the mollview projection of our estimates for the α_S index for both E and B. Figure B.2 displays the same but for the amplitude. Finally, Figure B.3 presents the same but for the ratio between B-to-E amplitudes.

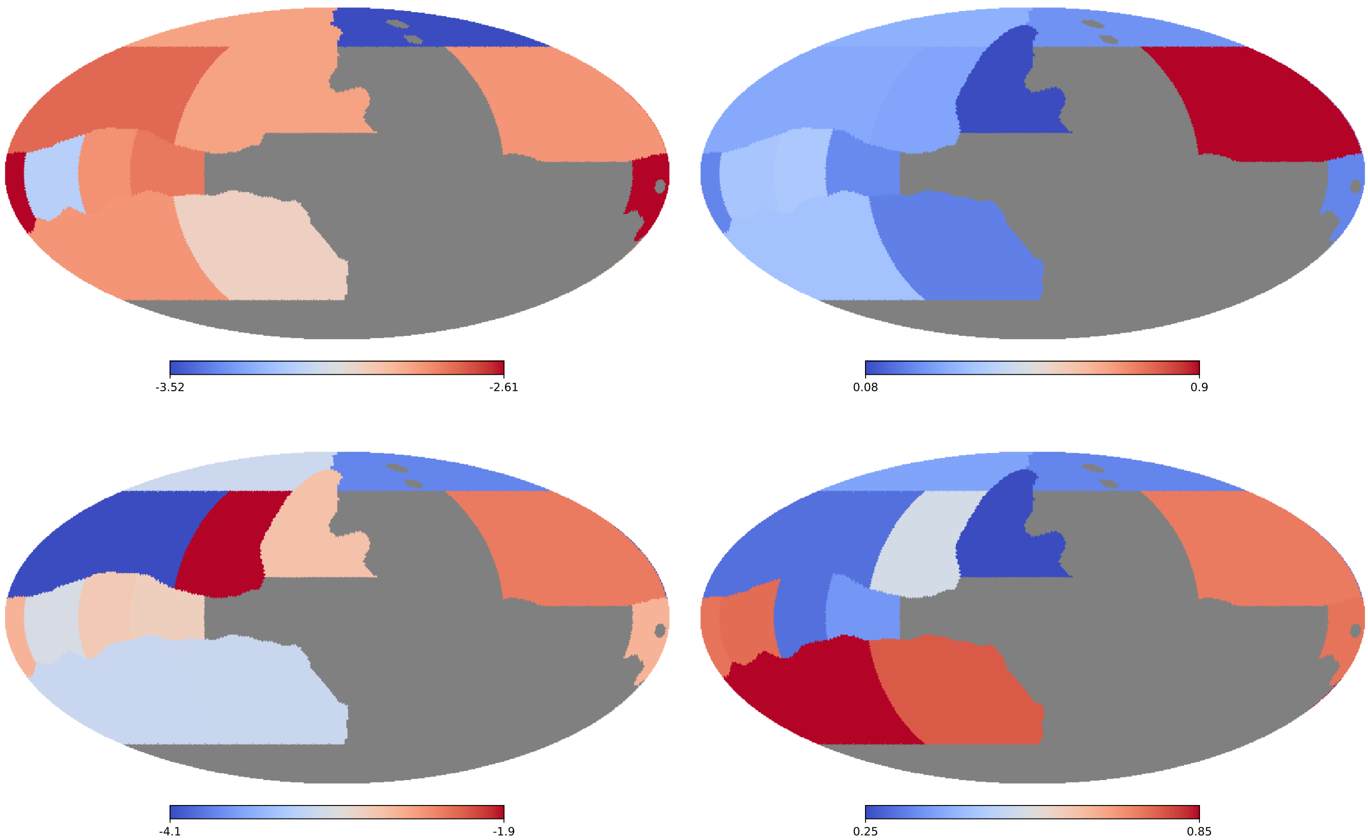

Fig. B.1: Mollview projection of our estimates for the α_S^{EE} (top pannel) and α_S^{BB} indeces in all the regions covered by the QUIJOTE MFI instrument at 11 GHz. The relative uncertainties (statistical plus systematic) for each region are shown in the right panel. The regions that we cannot analyze due to the QUIJOTE MFI covering are masked out in grey areas.

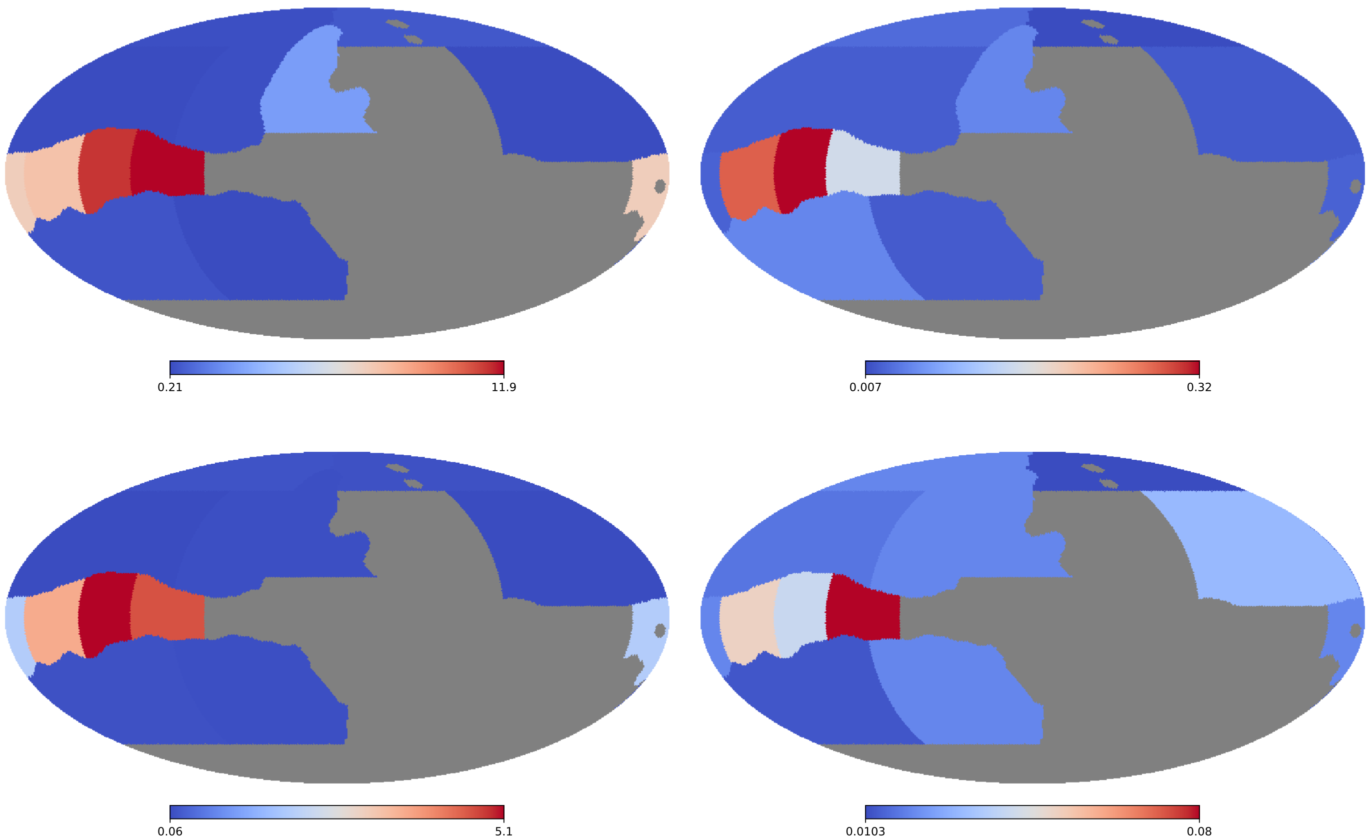

Fig. B.2: Mollview projection of our estimates for the A_S^{EE} (top pannel) and A_S^{BB} indeces in all the regions covered by the QUIJOTE MFI instrument at 11 GHz. The relative uncertainties (statistical plus systematic) for each region are shown in the right panel. The regions that we cannot analyze due to the QUIJOTE MFI covering are masked out in grey areas.

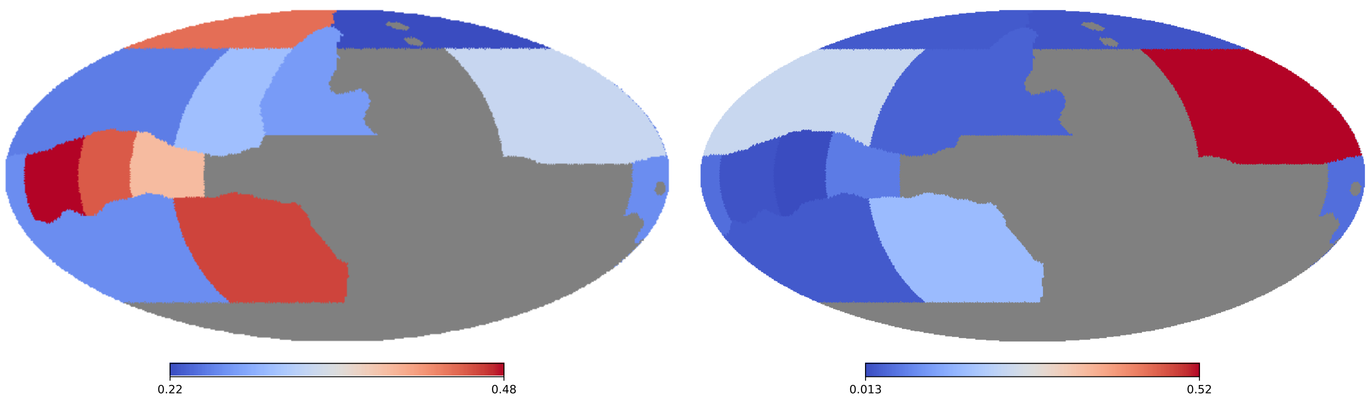

Fig. B.3: Mollview projection of our estimates for the ratio between amplitudes A_S^{BB}/A_S^{EE} in all the regions covered by the QUIJOTE MFI instrument at 11 GHz. Left panel: mean index for each region. The relative uncertainty (statistical plus systematical) for each region is shown in the right panel. The regions that we cannot analyze due to the QUIJOTE MFI covering are masked out in grey areas.